Dalton Transactions

Exceptional capability of nanosized CeO2 materials to "dissolve" lanthanide oxide established by time-gated excitation and emission spectroscopy

Journal:	*Dalton Transactions*
Manuscript ID:	DT-ART-11-2013-053254.R1
Article Type:	Paper
Date Submitted by the Author:	01-Feb-2014
Complete List of Authors:	Tiseanu, Carmen; National Institute for Laser, Plasma and Radiation Physics, Parvulescu, Vasile; University of Bucharest, Avram, Daniel; INFLPR, Cojocaru, Bogdan; University of Bucharest, Sanchez - Dominguez, Margarita; University of Monterrey,

Exceptional capability of nanosized CeO_2 materials to "dissolve" lanthanide oxides established by time-gated excitation and emission spectroscopy

Carmen Tiseanu,[*a] Vasile Parvulescu,[b] Daniel Avram,[a] Bogdan Cojocaru,[b] and Margarita Sanchez-Dominguez [c]

[*a] National Institute for Laser, Plasma and Radiation Physics, P.O.Box MG-36, RO 76900, Bucharest-Magurele, Romania; e-mail: tiseanuc@yahoo.com

[b] University of Bucharest, Department of Chemical Technology and Catalysis, 4–12 Regina Elisabeta Bvd., Bucharest, Romania

[c] Centro de Investigacion en Materiales Avanzados (CIMAV, S.C.), Unidad Monterrey, Alianza Norte 202, 66600 Apodaca, Nuevo Leon, Mexico;

Abstract

The atomic scale homogeneity of Ce and Zr oxygen bonds represents a main cause for the enhanced total Oxygen Storage Capability of CeO_2 - ZrO_2 (Ce/Zr = 1) as compared to that of CeO_2. Here, we demonstrate that the addition of 10% Eu^{3+} by wet impregnation on preformed nanosized CeO_2 - ZrO_2 (Ce/Zr = 1) followed by calcination induces a remarkable homogeneity of 10% Eu^{3+} - CeO_2 - ZrO_2 solid solution. By use of time-resolved emission and excitation spectroscopies, the improvement of the nanoscale chemical and structural homogeneity of 10% Eu^{3+} - CeO_2 - ZrO_2 calcined at 1000 compared to sample calcined at 750°C is demonstrated. Based on the comparison of luminescence properties of 10 % Eu^{3+} impregnated on preformed nanosized CeO_2 - ZrO_2 and CeO_2, we also show that the presence of zirconium does not only preserve the ability of cerium oxide to "dissolve" lanthanide oxide, but also determines an important stabilization of defects (oxygen vacancies) generated upon Eu^{3+} doping.

1. Introduction

There is large consensus in the literature that a single-phase solid solution of CeO_2 - ZrO_2 is preferable for the three-way catalysts (TWC) applications, in comparison with the microdomain or phase-segregated nonhomogeneous CeO_2 - ZrO_2 mixed oxides as the former is considered to have better textural stability and redox properties.[1] Usually, the thermal stability and redox properties of the mixed oxide solid solution can be promoted by adopting a suitable synthesis method, changing the atomic ratio of Ce/Zr and doping it with a foreign element. Doping of CeO_2 - ZrO_2 with trivalent RE (rare-earth) dopants can significantly affect their structural characteristics, improve the Oxygen Storage Capability (OSC) and the catalytic activity [2-5] by suppressing the phase decomposition of CeO_2 - ZrO_2 into *t* + *c/t"* phases. [3,5] The stabilization of the homogeneous CeO_2 - ZrO_2 solid solutions is dependent upon the nature and concentration of the RE dopant.[3] The RE ion with a larger size should be preferred in the low-doping concentration (y=0.08), whereas for the high doping concentration (y > 0.16), the dopant-oxygen vacancies associates lead to a decreased mobility of the oxygen vacancies. In the recent literature, there are many reports on the successful synthesis of CeO_2 - ZrO_2 solid solutions with high chemical and structural homogeneity with only few of them cited here. [1,3,6-10] Concerning the characterization of the homogeneity of CeO_2 - ZrO_2, this still represents a complex task. For the nanosized systems, the broadened X-ray diffraction (XRD) patterns obscure the occurrence of compositional inhomogeneity and/or multiple phases. Calcination in specific conditions, at 1273 K for 5h, followed by an appropriate XRD analysis may offer an effective criterion for definition of phase homogeneity, [11-13] though the presence of nanodomains cannot be ruled out. [14] In contrast with XRD, neutron diffraction is more effective in identifying the nanodomains of CeO_2 - and ZrO_2 -rich phases, [14] if the calcination temperature and time are carefully selected. [15] Atomic-scale electron imaging, nanometer-resolution electron energy loss spectroscopy, *in situ* environmental transmission electron microscopy and Raman technique combined with transmission electron microscopy and energy-dispersive spectrometry nano - analysis can also probe for the compositional and structural heterogeneities of CeO_2 - ZrO_2. [16 - 18] By using steady-state luminescence at single excitation wavelength the existence of domains ascribed to different phases of CeO_2 - ZrO_2 is established by using Eu^{3+} as a structural probe. [19] A different approach to that proposed in Ref. (20) is proposed by us[20], based on the analysis of Eu^{3+} luminescence in CeO_2 - ZrO_2 (Ce/Zr= 1) which is measured with both time and spectral resolution. Our study reveals the formation of CeO_2 - and ZrO_2 - rich nanodomains as well as the differences/ similarities between the local structure properties of CeO_2 and ZrO_2 parent oxides and CeO_2 - ZrO_2 mixed oxide.

Here , we report on a simple approach which integrates the synthesis, assessment of the nanoscale homogeneity and description of rare-earth dopant - defects interactions of a catalytically relevant, homogenous RE doped CeO_2 - ZrO_2 (Ce/Zr= 1). To generate homogeneous systems, the incorporation of the RE into CeO_2 - ZrO_2 is usually made *via* bulk doping since impregnation is expected to favour surface doping, especially for increased RE loadings. However, according to Corma et al., a homogenous solution can be formed even for high loadings of Zr^{4+} or La^{3+} (up to 30 %) added *via* wet impregnation on preformed nanosized CeO_2 followed by calcinations at 400 ºC. [21] The nanoscale dimension is crucial, since an analogous impregnation procedure applied to micrometre-sized CeO_2 leads to preferential surface doping. We demonstrate that, the nanosized mixed ceria - zirconia oxide is also capable to "dissolve" RE oxides such as Eu^{3+} oxide in concentration of 10 %. The selection of Eu^{3+} as the trivalent RE dopant was made on consideration of its outstanding luminescence sensitivity to the nearest oxygen ligands. We show that in contrast with 1% Eu^{3+} - CeO_2 - ZrO_2 [20], the impregnation of 10 % Eu^{3+} onto preformed CeO_2 - ZrO_2 leads to homogenous solid solutions upon calcinations and suppresses the effect of phase decomposition of CeO_2 - ZrO_2 into the *t + c/t"* phases. Finally, effects of Zr doping on the distribution of oxygen vacancies in CeO_2, considered to be responsible for the enhanced OSC properties of ceria-zirconia mixed oxides [22,23] are inferred from the comparison of the luminescence properties of 10% Eu^{3+} impregnated onto CeO_2 - ZrO_2 and CeO_2. The CeO_2 materials were synthesized under soft conditions by using the oil-in-water microemulsion reaction method [24] The 10% Eu^{3+} impregnated CeO_2 materials were calcinated in air at 750 and 1000 °C and investigated, by use of XRD, high-resolution transmission electron microscopy (HRTEM), micro - Raman and time-resolved emission/excitation spectroscopies and excited state-dynamics measurements.

2. Experimental Section

Materials. CeO_2 - ZrO_2 and CeO_2 nanocrystals were synthesized under soft conditions by using a recently developed oil-in-water microemulsion reaction method. [24] Eu^{3+} was added to the nanoparticles by wetness impregnation: 1 g of CeO_2 - ZrO_2 and CeO_2 were impregnated with the required amount of a 0.04 M aqueous solution of europium (III) chloride ($EuCl_3 \cdot 6H_2O$, Fluka) and left stirring overnight at 60 ºC. After that, the water was evaporated at 80 ^oC and the obtained powder was dried at 80 ºC in a drying oven for several hours. All samples were calcined under air *ex situ* conditions (at 750 and 1000 °C) by use of a heating rate of 4 ºC/ min.

Characterization. Powder X-ray diffraction (XRD) patterns were recorded on a Schimadzu XRD-7000 diffractometer using Cu K**α.** radiation (λ = 1.5418 Å, 40 kV, 40 mA) at a scanning speed of 0.20 degrees min^{-1} in the

20 – 90 degrees 2Θ range. DR-UV-Vis spectra of the catalysts were recorded with an Analytic Jena Specord 250 spectrometer equiped with an integrating sphere accessory. The spectra were recorded in reflectance units and were transformed in Kubelka–Munk remission function F(R). Raman analysis was carried out with a Horiba Jobin Yvon - Labram HR UV-Visible-NIR Raman Microscope Spectrometer, at 633, 514 and 488 nm and a catalytic cell with sample heating for *in-situ* measurements. The spectra were typically acquired under the following conditions: beam diameter of 1.0+5% mm, spot diameter of 0.5 μm, spatial resolution of 0.35 μm and spectral resolution of 2 $cm^{-1.}$ Elemental analysis was done by use of a X-ray fluorescence system with the following parameters: U=10-50kVp, I< 1 mA, X-ray targets: Mo and W, X-ray focusing by polycapillary lens or by dual W pin-holes and Si-PIN X-ray detector with energy resolution 149 eV at 5.9 keV. The photoluminescence (PL) measurements were carried out using a Fluoromax 4 spectrofluorometer (Horiba) operated in both the fluorescence and the phosphorescence mode. The repetition rate of the xenon flash lamp was 25 Hz, the integration window varied between 0.1 and 0.5 s, the delay after flash varied between 0.03 and 25 ms, and up to 30 flashes were accumulated per data point. For excitation spectra, the slit bandpass varied from 5 to 29 nm while in emission the slit bandpass varied from 0.3 nm to 1 nm. The PL decays were measured by using the "decay by delay" feature of the phosphorescence mode. Time resolved emission spectra (TRES) were recorded at room temperature using a wavelength tunable NT340 Series EKSPLA OPO (Optical Parametric Oscillator) for samples excitation at 350-360 nm, 395-396 nm, 448-492 nm, 525-532 nm operated at 10 Hz as excitation light source. The tunable wavelength laser had a narrow linewidth < 4 cm^{-1} with a scanning step varying of 0.1 nm. As detection system an intensified CCD (iCCD) camera (Andor Technology) coupled to a spectrograph (Shamrock 303i, Andor) was used. The TRES were collected using the box car technique. PL was detected in the spectral range of 550 nm < λ_{em} < 750 nm with a spectral resolution which varied from 0.05 nm to 0.88 nm and the input slit of the spectrograph was set to 10 μm. The temperature of the iCCD was lowered at -20 ^{0}C for a better signal to noise ratio. For all measurements done by iCCD, a cut off filter of 532 nm was used to protect the detector from the excitation light. The delay after pulse varied from 0.01 up to 40 ms, with a 100-500 μs gate and 100 - 200 accumulations per pulse depending on the signal to noise ratio. All measurements were performed at room - temperature.

3. Results and Discussion

3. 1. Homogeneity assessment by XRD, Raman and HRTEM analysis. Phase identities and purities of undoped and Eu^{3+}- doped CeO_2 - ZrO_2 calcined at 750 and 1000 °C were investigated by XRD. The samples are denoted as CZ - 750 and CZ - 1000 for the undoped CeO_2 - ZrO_2; CZE - 750 and CZE - 1000 for Eu^{3+} - doped CeO_2 - ZrO_2 calcined at 750 and 1000 °C, respectively. For the undoped sample calcined at 750 °C (CZ - 750), the symmetrical diffraction peaks can be indexed either as cubic (c) or pseudocubic (t'') phase evidencing for the formation of solid solution (PDF card 00-038-1439). The crystallite size and lattice constant are 6.2 nm (as estimated by use of the Debye-Scherer Equation) and 5.29 Å, respectively. For the undoped CeO_2 - ZrO_2 calcined at 1000 °C (CZ - 1000), the splitting of diffraction peaks is evident, indicating for phase segregation as illustrated with zoomed region around 2θ = 48 degrees shown in the Inset of Figure 1. The new peaks can be indexed as $Ce_{0.75}Zr_{0.25}O_2$ phases enriched in ceria (PDF 00-028-0271).

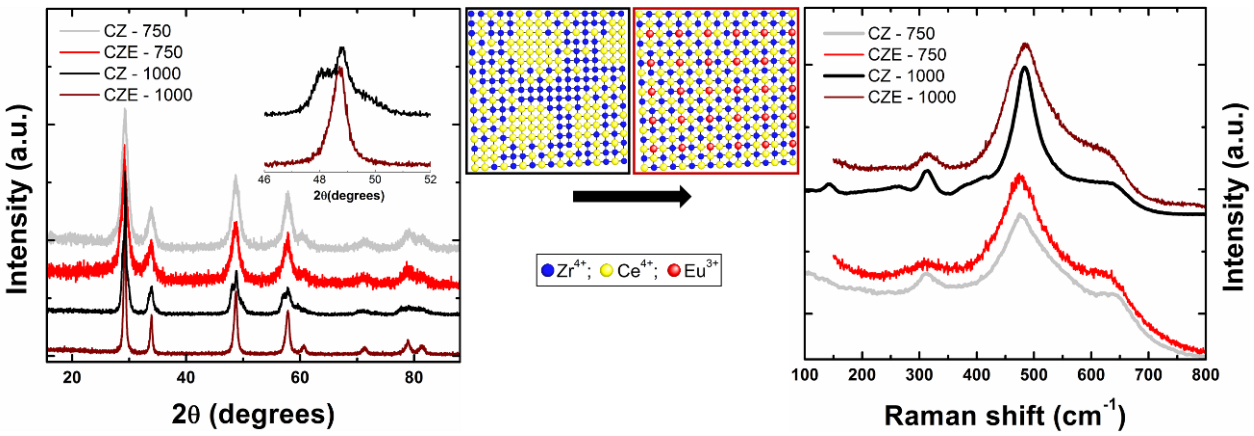

Fig. 1. XRD patterns (Left) and Raman spectra (Right) of undoped and 10% Eu^{3+} - doped CeO_2 - ZrO_2 calcined at 750 (CZ - 750 and CZE - 750) and 1000 °C (CZ - 1000 and CZE - 1000). Left Inset: zoomed region of XRD patterns around 2θ = 48° for CZ - 1000 and CZE - 1000. Middle: Schematic illustration of cation - cation network for CZ - 1000 and CZE - 1000 which shows that, in the absence of Eu^{3+}, Ce and Zr rich domains are formed whereas 10% Eu^{3+} impregnation induces a homogeneous solid solution upon calcinations at 1000 °C.

For the Eu^{3+} - CeO_2 - ZrO_2, the symmetrical XRD patterns can be indexed either as cubic or as pseudocubic (t'') phase (from PDF card 00-038-1439) confirming the formation of solid solution at both 750 and 1000 °C. Crystallite

sizes of 6.3 and 18.9 nm and lattice constants of 5.293 and 5.305 Å are estimated for CZE - 750 and CZE - 1000, respectively. It is evident that the XRD lines related to Eu_2O_3 are not detected. For the undoped and Eu^{3+} - doped CeO_2 - ZrO_2 samples calcined at 750 °C, the small crystallite size of ~ 6 nm is small enough to obscure the different arrangements of oxygen sublattice or the presence of a multi-phase system at a nanoscale level. [25] Furthermore, since the t" phase has also a cubic cation sublattice, it cannot be discriminated against the cubic phase by XRD analysis. On the other side, the t″ form is tetragonal in the oxygen sublattice because the oxygen atoms are displaced along the *c* axis from the regular 8*c* position of the cubic phase. Therefore c and t" phases are usually discriminated by use of Raman scattering which is sensitive to small oxygen displacements. [26] The Raman spectrum of CZ - 750 is broad suggesting a defective structure characteristic of the pseudocubic nature (Figure 1). The dominating band at 475 cm^{-1} is related to the F_{2g} mode of the cubic fluorite-like structure, followed by weaker bands at ~ 314 and 630 cm^{-1} related to the displacement of oxygen atoms from their ideal fluorite lattice positions and to a non-degenerate longitudinal optical (LO) mode of ceria induced by the oxygen vacancies in the ceria lattice, respectively. The Raman spectrum of CZ - 1000, the narrowing of the F_{2g} band peaked at 483 cm^{-1} together with the presence of a weak band around 260 cm^{-1}, characteristic of t - phase confirm the phase separation with tetragonal and cubic phase components as observed with XRD. For Eu^{3+} doped CeO_2 - ZrO_2, single phase of pseudocubic origin is determined at both calcinations temperatures. According to literature, stabilization of the pseudocubic phase instead of the stable tetragonal phase, can be related to the small crystallite size[27] of both undoped and Eu^{3+} doped samples calcined at 750 ºC (ca. 6 nm) while the presence of 10 % Eu^{3+}, is sought to stabilize the lattice defects and improve their distribution within the lattice. [3] Raman bands related to Eu_2O_3 phase are not observed, as, for example, the cubic structure of europium oxide displays a strong F_{2g} band around 340 cm^{-1}. [28] Since Raman spectroscopy is able to detect luminescence from unintentional doped lanthanides in a concentration level as low as ppm, [29] we take a close look to Raman spectra of CZE - 750 and CZE - 1000 measured in the extended range, up to 4000 cm^{-1}. The spectra were excited at 488 and 514 nm, both wavelengths being reported to excite Eu^{3+} emission in ceria and zirconia materials. [30,31] As illustrated in Figure S5 in the Supplemental Info (514 nm excitation), several narrow and relative intense lines are observed in the range of spectral shift of ~ 2000 to 4000 cm^{-1}. As it will be discussed next, these lines correspond exclusively to the $^5D_0$ - $^7F_{0,\,1,\,2}$ luminescence transitions of Eu^{3+} located in the Ce/Zr sites of CeO_2 - ZrO_2 lattice. Finally, X-ray fluorescence analysis does not evidence the presence of other metal impurities.

HRTEM analysis was consistent with the results from XRD and RAMAN. Figure 2 (Left) shows the HRTEM images of CZ - 750 (Fig. 2(a) and 2(b)), CZE - 750 (Fig. 2(c) and 2(d)) and CZE - 1000 (Fig. 2(e) and 2(f)). The approximate sizes of the nanocrystals were 8 nm for CZ - 750, 40 – 80 nm for CZ – 1000, 10 nm for CZE - 750 and 20 - 50 nm for the CZE - 1000.

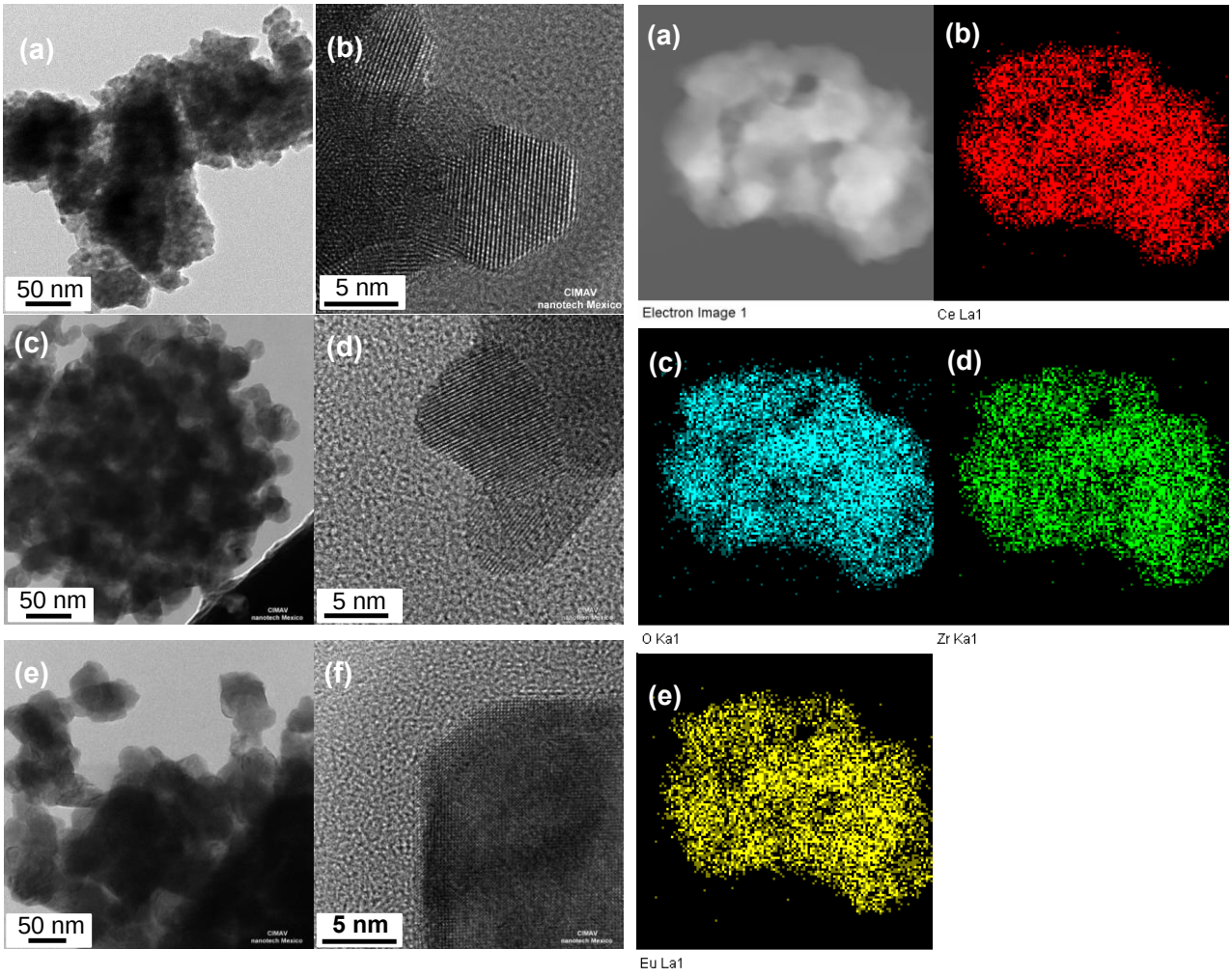

Fig. 2. Left: HRTEM images of CZ - 750 (a, b); CZE - 750 (c, d) and CZE - 1000 (e, f) and Right: Elemental mapping of CZE - 1000 sample carried out by EDS. (a) Electron image; (b) Ce; (c) O; (d) Zr; (e) Eu.

The shape of the nanocrystals was mainly facetted, with the presence of some less defined particles with more rounded edges. HRTEM revealed crystalline features, and careful analysis (carried out performing the fast Fourier transform (FFT) of the HRTEM images, crystal by crystal) indicated that whilst the undoped sample CZ - 750 and

especially CZ - 1000 (not shown) presented characteristic d - spacings for three different structures (cubic ceria, tetragonal structure, and a predominant cubic ceria-zirconia), the doped samples CZE - 750 and CZE - 1000 were generally consistent with d - spacings characteristic of cubic/pseudocubic ceria-zirconia only. This analysis permitted to confirm the homogeneity of the 10 % Eu^{3+} - CeO_2 - ZrO_2 samples in terms of their crystallinity, as compared to the undoped CZ - 750 and especially CZE - 1000 samples which presented evidence of several crystalline phases. The results contrast our previous study which revealed that when samples were doped with only 1 % Eu^{3+}, several crystalline phases coexisted, in particular for the sample calcined at 1000 ºC. [20] On the other hand, elemental mapping was carried out on the CZE - 1000 sample by energy dispersive spectroscopy (EDS). The results shown in Figure 2 Right confirmed that the elemental distribution of Ce, Zr, Eu and O was remarkable homogeneous. FFT analysis of individual crystals and selected area electron diffraction (SAED) images are illustrated in the Figures S1 - S4.

3.2. Homogeneity assessment by luminescence analysis. To check further on the true homogeneous nature of CZE -750 and CZE - 1000 suggested by XRD, Raman and HRTEM investigations, we compare the Eu^{3+} luminescence in the two samples. It is well-known that Eu^{3+} luminescence is strongly sensitive to location (surface or inner lattice sites) and the symmetry of the nearby oxygen environments[32,33] which means that the local scale sensitivity is smaller than 3 Å.

The luminescence of Eu^{3+} in CZE – 750 and CZE – 1000 is excited by a narrow, nanosecond pulsed laser with a tunable excitation spanning the UV to Vis spectral range.[20] As shown in Figure 3, except for a weak, broad absorption at ~ 330 nm, only the f - f absorptions induce Eu^{3+} emission (at ~ 455 - 475 nm and ~ 520 - 540 nm corresponding to the $^7F_0$ - $^5D_2$ and $^7F_{0,\ 1}$ - $^5D_1$ transitions, respectively.). For each excitation wavelength, we have measured the time evolution of the emission spectra at delays after the laser pulse which increased from few μs up to 10 ms. Along these lines, we could established that for a delay greater than 5 ms, basically no changes of the (peak normalized) time resolved emission spectra occurred, identifying thus only the distinct Eu^{3+} sites. Among over 50 measured PL spectra obtained by varying the excitation wavelength from 330 to 536 nm, at least four (sample calcined at T= 750 °C) and three different spectra (sample calcined at T= 1000 °C) could be separated and linked to Eu^{3+} in distinct Ce/Zr lattice sites (Figure 3). Similar to our previous study on 1 % Eu^{3+} - CeO_2 - ZrO_2 [20] the spectra were differentiated by the relative intensities of the emissions centred at ~ 591 and 605 nm, their peak positions and widths (Figure S6 and S7 and Tables S1 and S2). The emission at 591 and 605 nm correspond to the electric and

magnetic dipole $^5D_0$ - $^7F_2$ and $^5D_0$ - $^7F_1$ transitions, respectively with their intensity ratio R= I($^5D_0$ - $^7F_2$)/ I($^5D_0$ - $^7F_1$), named as asymmetry ratio, being an effective indicator for the local symmetry of the Eu^{3+} - oxygen coordination polyhedron. [34,35] The higher this ratio, the closer is the local symmetry around Eu^{3+} to an inversion centre. To discard the error introduced by the very weak intensity of the $^5D_0$ - $^7F_2$ lines in the range of ~ 610 - 640 nm, only the integrated intensity corresponding to 605 nm based emission was considered in the estimation of the asymmetry ratio.

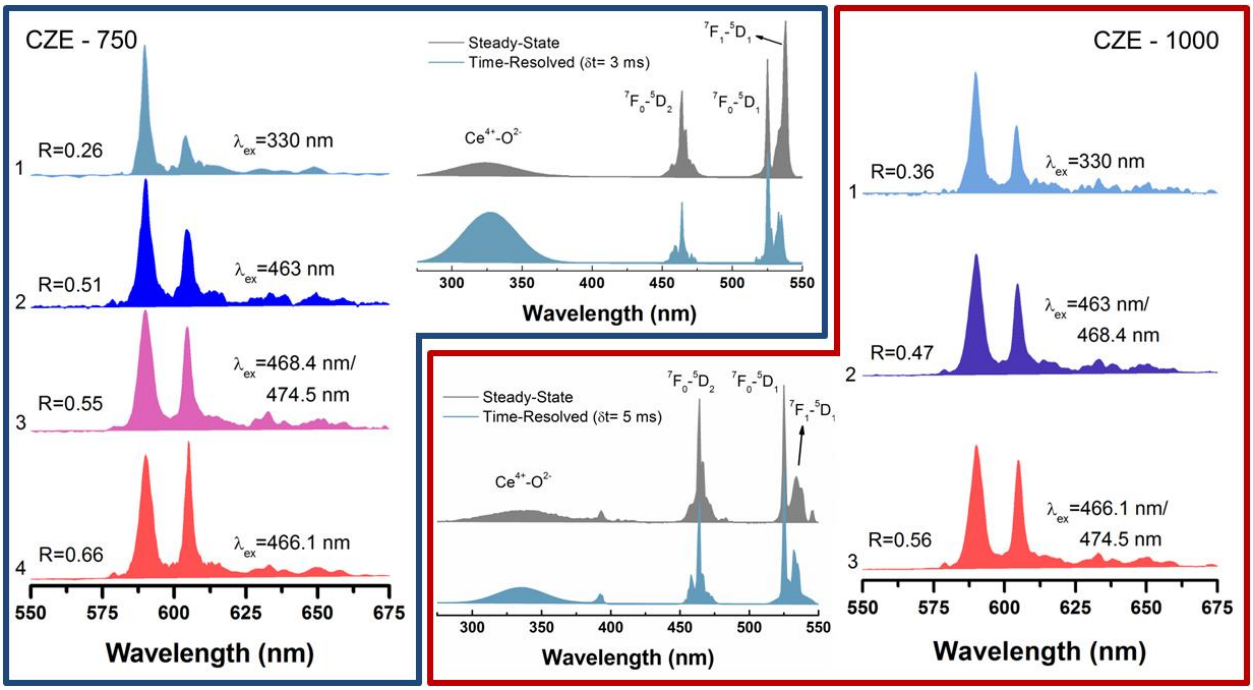

Fig. 3. Emission and excitation spectra of 10 % Eu^{3+} - CeO_2 - ZrO_2 calcined at 750 (CZE 750, Left) and 1000 °C (CZE – 1000, Right). The emission spectra were measured by use of a delay time of 5 ms after the laser pulse. The excitation spectra were measured under steady-state and time-resolved mode with delay times after the lamp pulse of 3 ms (750 °C) and 5 ms (1000 °C). All emission spectra were normalized at 591 nm corresponding to peak intensity of the $^5D_0$ - $^7F_1$ transition. The excitation spectra were normalized at 526 nm corresponding to peak intensity of the $^7F_0$ - $^5D_1$ transition.

The thus estimated R values associated to spectra 1 - 4 (CZE - 750) and 1- 3 (CZE - 1000) increased from 0.26 to 0.66 and from 0.36 to 0.56, respectively as noted also in Figure 3. To relate the local symmetry properties derived from the emission spectra of CZE - 750 and CZE - 1000 to compositional and/or structural homogeneity of the

mixed oxide, we briefly recall that the tetragonal ZrO_2 is derived *via* distortion of the cubic fluorite. CeO_2 crystallizes in a cubic fluorite structure (*Fm*3*m* space group) where each Ce^{4+} cation is eight-fold coordinated by oxygen anions located at the corner of a cube. When part of Ce ions are substituted for Zr the defects generated in the ceria–zirconia lattice lead to the distortion of the oxygen sublattice since the ionic radius of Zr (0.84 Å) is smaller compared to that of Ce^{4+} (0.97 Å), both in eight-coordination. [36] The oxygen displacement along the *c* axis from the cubic fluorite regular position, decrease with ceria content determining a progressive change of the symmetry of solid solutions from tetragonal to cubic with the increase of the Ce to Zr atomic ratio. [37] In CeO_2, Eu^{3+} substitutes for the eight-folded Ce^{4+} sites with O_h inversion symmetry and thus, its emission fingerprint consist of a strong emission at 591 nm, corresponding to the allowed magnetic dipole $^5D_0$ - $^7F_1$ transition. In tetragonal ZrO_2, the eight-folded Zr^{4+} has two sets of short (2.17 A) and long (2.36 A) Zr - O bond lengths which define a D_{2d} inversion less symmetry at the cation sites. [38] The emission fingerprint of Eu^{3+} substituting for Zr in the tetragonal ZrO_2 is given by two emissions bands with comparable intensity, at 591 nm (corresponding to the merging of the two allowed $^5D_0$ - $^7F_1$ transition lines) and ~605 nm (which is the strongest among the four allowed $^5D_0$ - $^7F_2$ lines).[20]

The emission spectra illustrated in Figure 3 vary in the order of increasing label from a more ceria to a more tetragonal zirconia emission indicating for the departure from the nominal, unitary Ce/Zr composition ratio on the atomic scale. Surface type emission of Eu^{3+}, with strongly distorted shape is also detected, but it is quenched after few hundred μs after the laser pulse and has only minor contribution to the total emission as exemplified with spectra in Figure 4. We should emphasize that XRD and Raman data were not able to reveal any difference between Eu^{3+} - CeO_2 - ZrO_2 samples calcined at 750 and 1000 °C, other than those due to increased crystallization. In contrast, as shown below, the luminescence analysis in terms of time-resolved emission/excitation spectra and excited - state dynamics measurements demonstrates a higher homogeneity of CZE - 1000 compared to CZE - 750.

First, for CZE - 1000, the values of the asymmetry ratio appear to be confined into a narrower range, of 0.36 - 0.56 compared to 0.26 - 0.66 for CZE - 750. This result confirms a narrower distribution of Eu^{3+}- oxygen environments in CZE - 1000 compared to CZE - 750. Second, the comparison of the excitation spectra measured in the steady-state and time-resolved modes evidence that the excitation modes of Eu^{3+} emission in CZE - 750 and CZE - 1000 are not similar. In the latter measurement mode, the excitation spectra were acquired by using a delay after the lamp pulse (3 and 5 ms at T= 750 and 1000 °C, respectively). The delay values were chosen in order to reduce the contribution of the shorter-lived emission of Eu^{3+} in tetragonal like sites and to separate better the longer-lived emission of Eu^{3+}

located in the more symmetrical, ceria like sites. It is obvious from the spectra in Figure 3 that the time-resolved excitation spectrum of CZE - 750 is strongly different to spectrum measured in the steady-state mode, with a strong enhancement in the band intensity at 330 nm relative to intensity of f - f absorptions.

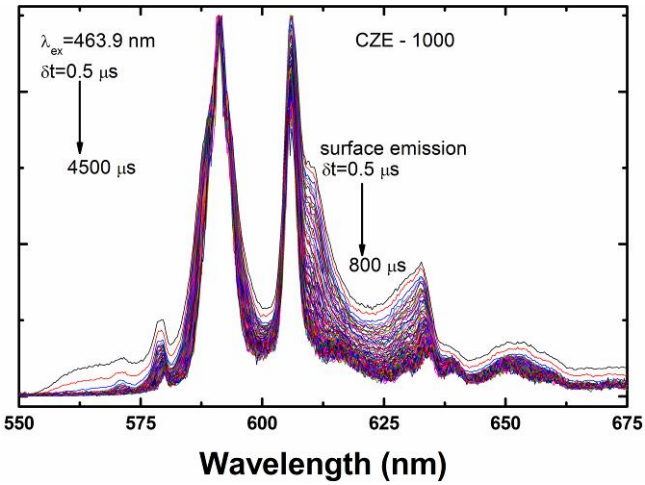

Fig.4. Evolution of luminescence spectra of 10 % Eu^{3+} - CeO_2 - ZrO_2- 1000 (CZE - 1000) with delay time after the laser pulse. The spectra show only a minor contribution for the surface type emission to the overall emission.

It is established by several authors including some of us[30,39] that the ceria host *via* its Ce^{4+} to O^{2-} charge-transfer (CT) band located into UV region, sensitises strongly the Eu^{3+} emission. We assign therefore the broad absorption band around 330 nm to the CT band of ceria. The stronger intensity of this band measured for CZE - 750 than CZE - 1000 can be taken as proof for the presence of ceria like environments at Eu^{3+} sites, i.e. onset of phase segregation. Finally, the excited state dynamics of Eu^{3+} measured on the $^5D_0$ - $^7F_1$ transition (591 nm) upon excitation into CT band and f-f absorption (corresponding to the $^7F_0$ -$^5D_2$ transition at 466 nm) is compared for CZE - 750 and CZE - 1000 (Figure 5). In principle, for Eu^{3+} distributed on unique site, the luminescence decay should approach a single exponential, irrespective of the excitation wavelength. By using similar excitation/emission conditions, the measured luminescence decays display a clear dependence on the excitation wavelength for both CZE - 750 and CZE - 1000 samples (Figure 5). However, the variation of the average PL lifetimes with excitation wavelength is significantly diminished in CZE - 1000 compared to CZE - 750. Specifically, for CZE - 750, the average PL lifetimes differ by a maximum factor of two (i.e. 1.89 and 0.88 ms) compared to less than 1.5 (i.e. 3.21 and 2.13 ms) for CZE - 1000 when varying the excitation wavelength from the CT band of CeO_2 to f - f absorption of Eu^{3+}. Further, the shapes of

the PL decays approach more a single exponential for the case of CZE - 1000 compared to CZE - 750 which give a further confirmation of the more homogeneous Ce/Zr - oxygen environments in CZE - 1000 compared to CZE - 750.

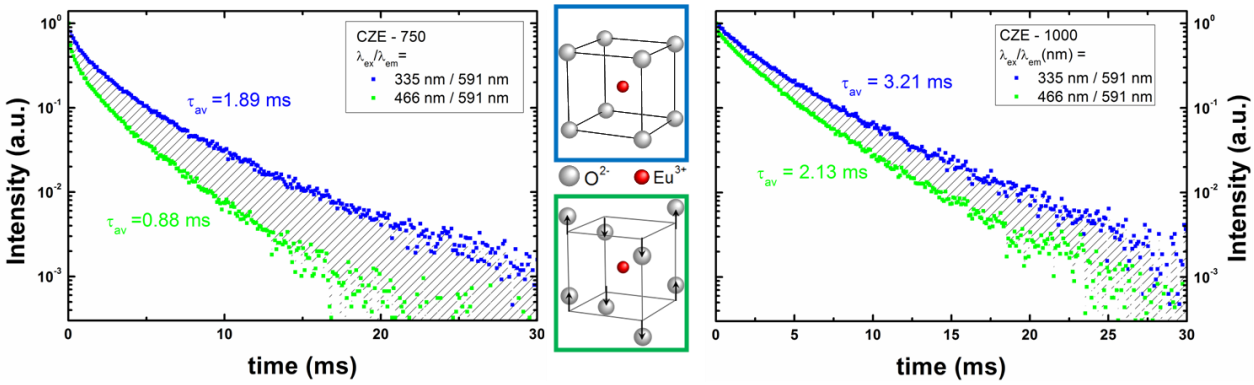

Fig. 5. Dependence of the PL decays of 10 % Eu^{3+} - CeO_2 - ZrO_2 calcined at 750 (CZE – 750, Left) and 1000 °C (CZE – 1000, Right) on the excitation wavelength. Middle: Schematic representation of Eu^{3+} in cubic and pseudocubic lattice (t" phase) with the oxygen anions displaced from the regular 8*c* position of the cubic phase.

The results contrast those obtained with 1 % Eu^{3+} - CeO_2 - ZrO_2[20] where for the sample calcined at 1000 °C, the emission of Eu^{3+} reveals both structural and compositional inhomogeneity. [28] Since the CeO_2 - ZrO_2 with a Ce/Zr atomic ratio close to unity has the composition which is most easily prone to segregation and the addition of Eu^{3+} in concentration of 1 % is supposed to influence only weakly the structure of the CeO_2 - ZrO_2 host, both tetragonal and ceria like feature were observed in the XRD, HRTEM, Raman and luminescence properties of 1 % Eu^{3+} - CeO_2 - ZrO_2 calcined at 1000 ºC.[20]

3. 3. Effects of Zr doping on the oxygen vacancy distribution in CeO_2. Since luminescence of Eu^{3+} is known to be very sensitive to nearest neighbour (NN) oxygens and according to EXAFS data, the (NN) neighbor environment responds the most strongly to a change in the number of oxygen vacancies[40] the shape of luminescence can be related to Eu^{3+} - oxygen vacancy interactions. The aliovalent substitution of Ce/Zr cations with 10 % Eu^{3+} generate a great amount of defects (mainly oxygen vacancies[41]) which interact with Eu^{3+} either in the nearest-neighbour (NN) or next nearest neighbour (NNN) modes. The emission of Eu^{3+} in CZE - 750 and CZE - 1000 is given exclusively by the distant interactions with oxygen vacancy (NNN mode). In the opposite scenario, for the case of a defect localized at the NN position to Eu^{3+} rather to Ce or Zr cations, the local symmetry at Eu^{3+} sites will be distorted from the tetragonal symmetry characteristic of pseudocubic CZE - 750 or CZE - 1000. The corresponding emission will be

then dominated by a much stronger $^5D_0$ - $^7F_2$ emission compared to $^5D_0$ - $^7F_1$ emission, with values for the asymmetry ratio greater than 1 which contrasts with spectra illustrated in Figure 3. To gain more in depth knowledge on the Eu^{3+} - oxygen interactions in the mixed oxide, we compare the emission properties of 10 % Eu^{3+} doped CeO_2 - ZrO_2 calcined at 1000 °C (CZE - 1000) to those of 10 % Eu^{3+} doped CeO_2. The 10 % Eu^{3+} doped CeO_2 sample is obtained *via* wet impregnation on preformed CeO_2 nanoparticles synthetized by a similar method and subjected to calcination in air at 1000 °C in similar conditions to those used for CZE - 1000. First, the homogeneity of 10 % Eu^{3+} doped CeO_2 is readily confirmed by XRD and Raman analysis (Figure 6 Left).

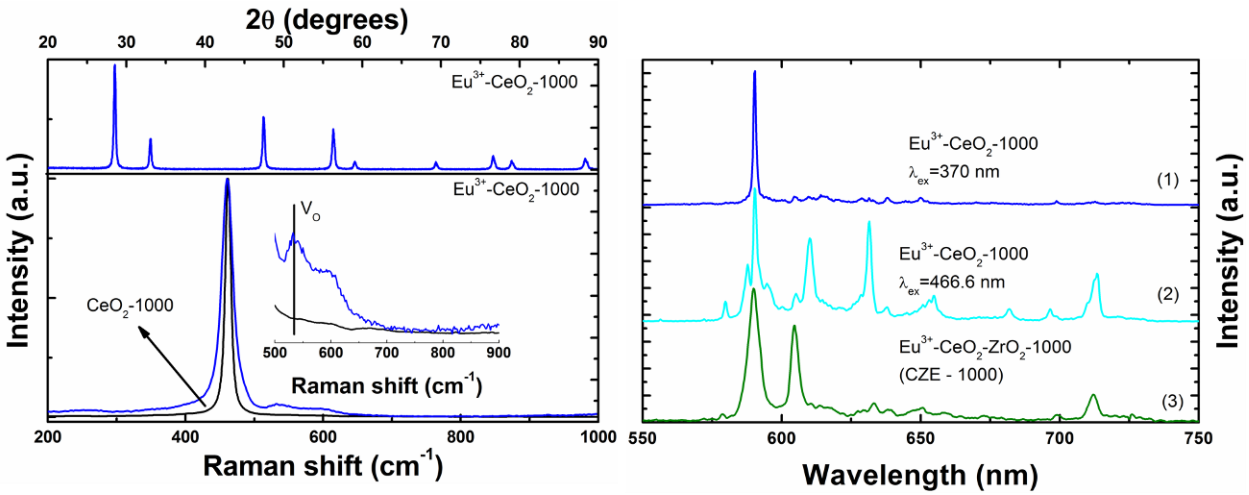

Fig. 6. Structural (Left) and emission (Right) properties of 10 % Eu^{3+} - CeO_2 - 1000. Eu^{3+} was added *via* wet impregnation on CeO_2 followed by calcinations at 1000 °C. Left: Top: XRD patterns of 10 % Eu^{3+} - CeO_2 - 1000 which show only the reflections of the cubic fluorite phase with a crystallite size of 38 nm; Bottom: Raman spectra of undoped and 10 % Eu^{3+} - CeO_2 - 1000. Right: Spectrum 1 illustrates the fingerprint emission of isolated Eu^{3+} (with NNN interaction to oxygen vacancy); spectrum 2 is a superposition of Eu^{3+} emissions due to NNN and NN interactions to oxygen vacancy and spectrum 3 refers to the "average" spectrum of Eu^{3+} in CeO_2 - ZrO_2 – 1000 (see also Figure 3).

Only highly symmetric, cubic, fluorite type XRD patterns, with no diffraction peaks attributable to other components or phases are observed. The shape of the Raman spectrum is dominated by the narrow F_{2g} mode (at 473 cm^{-1}) characteristic of the fluorite lattice. Generation of the oxygen vacancies induced by 10 % Eu^{3+} doping in the CeO_2

lattice can be assessed readily from the increased intensity of ~ 540 cm^{-1} band (denoted as V_o) compared to undoped CeO_2 [42]. Association between an oxygen vacancy and a RE dopant is well established in fluorite-structured materials by means of atomistic simulations and/or in experiments. [41,43,44] Recent calculations established that RE dopants larger than Gd^{3+} (such as Eu^{3+}) repel the oxygen vacancy from NN sites leading to increased ionic conductivity. [41,43-46] The luminescence of 10 % Eu^{3+} - CeO_2 agree with two main Eu^{3+} centres differentiated by their interaction modes with oxygen defects (Figure 6 Right): spectrum 1 corresponds to isolated Eu^{3+}, i.e. Eu^{3+} located in the NNN position towards an oxygen vacancy. Its chemical environment retains closely that of CeO_8 cube and therefore the emission is dominated by the magnetic dipole $^5D_0$ - $^7F_1$ transition at 591 nm characteristic of Eu^{3+} in centrosymmetric sites.[30] Spectrum 2 is a superposition of emissions corresponding to isolated and Eu^{3+} oxygen vacancy associates (i.e. Eu^{3+} located in the NN position to oxygen vacancy). The presence of an oxygen vacancy in the nearest oxygen shell of Eu^{3+} distorts severely the cubic symmetry by removing the inversion centre and decreasing the coordination number from 8 to 7 or even 6. [47] The $^5D_0$ - $^7F_2$ emission lines at 611 and 632 nm can be regarded as fingerprint emission for Eu^{3+} - oxygen vacancy associates in CeO_2. [48] Finally, spectrum (3) corresponds to the "average" emission of CZE - 1000. It can be readily observed that the presence of Zr induces broader emission widths in CeO_2 - ZrO_2 than CeO_2 (~ 2.3–2.7 compared to ~ 0.8 nm for the 591 nm peaked emission), which proves for the more disordered oxygen environments around cation sites in the mixed oxide compared to ceria as previously observed with 1 % Eu^{3+} - CeO_2 - ZrO_2. The larger spatial distribution of oxide ions in CeO_2 - ZrO_2 with a Ce/Zr = 1 compared to CeO_2 is considered one of the key parameters leading to increased catalytic activity in the mixed oxide. [49] The major difference between spectra 1 - 3 in Figure 6 Right, concern the absence of emission characteristic of Eu^{3+}- defects associates (i.e. lines at 611 and 632 nm) in CeO_2 - ZrO_2. We explain the absence of the localized defects at the Eu^{3+} sites in CeO_2 - ZrO_2 to Zr which acts as a scavenger for the oxygen vacancies. This behavior was previously assigned to the difference of the stability of MO_8 unit with different cations (M= Zr and Ce) in fluorite crystal lattice, where the degree of stabilization of the oxygen vacancy was suggested to be higher for Zr than Ce.[50]

4. Conclusions

Here we demonstrate that the addition of 10 % Eu^{3+} by wet impregnation onto preformed nanosized CeO_2 - ZrO_2 followed by calcination simultaneously induces and probes *via* luminescence for a remarkable chemical and

structural homogeneity of 10 % Eu^{3+} - CeO_2 - ZrO_2 solid solution. The effects of Zr presence on the distribution of oxygen vacancies in CeO_2 are inferred from the comparison of the luminescence properties of 10 % Eu^{3+} in CeO_2 - ZrO_2 and CeO_2. Our results may of relevance for a broad range of materials for which the knowledge of local structure properties, defects formation and their stabilization play a key role in the various catalytic and electrochemical applications.

Acknowledgements

CT, BC and DA acknowledge financial support from the Romanian National Authority for Scientific Research (CNCS-UEFISCDI) (project number PN-II-ID-PCE-2011-3-0534). CT also acknowledges COST Action CM1104 "Reducible oxide chemistry, structure and functions". MSD is grateful to CONACYT (CB project with grant number CB2011/166649) and NaNoTeCh, the National Nanotechnology Laboratory of Mexico. Cesar Leyva Porras (CIMAV, S.C.) is acknowledged for measurements and assistance with HRTEM and EDS mapping.

Keywords: cerium, zirconium, local structure, oxygen vacancy, homogeneity, europium, luminescence

ASSOCIATED CONTENT

Additional fast Fourier transform (FFT) analysis, selected area electron diffraction images, Raman and luminescence spectra. This material is available free of charge via the Internet at http://pubs.acs.org**.**

Graphical Abstract

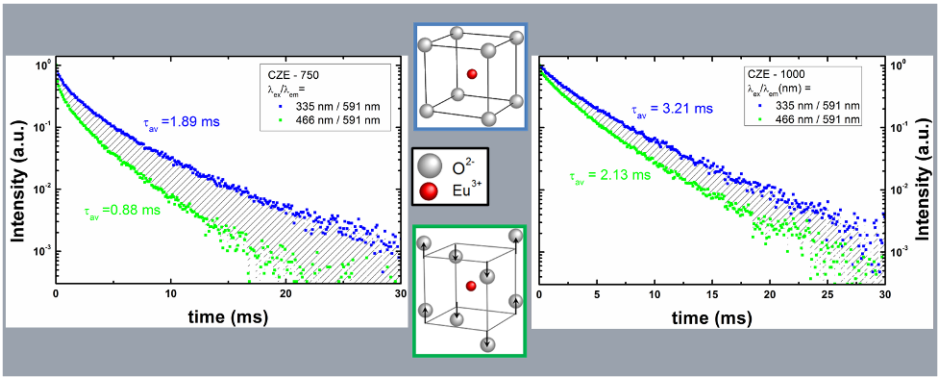

References

1. J. Kašpar, P. Fornasiero and N. Hickey, *Catal. Today* 2003, **77**, 419-449
2. P. Vidmar, P. Fornasiero, G. Gubitosa and M. Graziani, *J. Catal.*1997, **171**, 160-168
3. R. Si, Y.–W. Zhang, L.M. Wang, S.J, Li, B. X. Lin, B.X.; W. S. Chu, Z. Y. Wu and C. H. Yan, *J. Phys. Chem. C.* 2007, **111**, 787-794
4. H. He, H. X. Dai, K. W. Wong, C. T. Au, *Appl. Catal., A: Gen.* 2003, **251**, 61
5. L.N. Ikryannikova, A.A. Aksenov, G.L. Markaryan, G.P. Murav'eva, B.G. Kostyuk, A.N. Kharlanov and E. V. Lunina, *Appl. Catal., A:Gen.* 2001, **210**, 225
6. J. Kašpar and P. Fornasiero, *J. Solid State Chem.* 2002, **171**, 19-29
7. R. Si, Y.W. Zhang, S. Li, B.X. Lin and C.H. Yan, *J. Phys.Chem. B* 2004, **108**, 12481-12488
8. E. Mamontov, T. Egami, R. Brezny, M. Koranne and S. Tyagi, *J. Phys. Chem. B* 2000, **104**, 11110-11116
9. M. Hirano, T. Miwa and M. Inagaki, *J. Solid State Chem.* 2001, **158**,112-117
10. M. Yashima, T. Sekikawa, D. Sato, H. Nakano and K. Omoto, *Cryst. Growth Des.* 2013, **13**, 829-837
11. C.E. Hori, H. Permana, K.Y.S. Ng, A. Brenner, K. More, K.M. Rahmoeller and D.N. Belton, *Appl. Catal. B* 1998, **16**, 105-117
12. G. Colon, F. Valdivieso, M. Pijolat, R.T. Baker, J. J. Calvino and S. Bernal, *Catal. Today* 1999, **50**,271-284
13. P. Fornasiero, R. Di Monte, J. Kaspar and T. Montini, *Stud. Surf. Sci. Catal.* 2000, **130**, 1355-1360
14. E. Mamontov, R. Brezny, M. Koranne and T. Egami, *J. Phys. Chem. B* 2003, **107**,13007-13014
15. R. Di Monte and J. Kašpar, *J. Mater. Chem*. 2005, **15**, 633-648
16. R. Wang, P.A. Crozier, R. Sharma and J.B. Adams, *J. Phys. Chem. B* 2006, **110**, 18278-18285

17. R. Wang, P.A. Crozier, R. Sharma and J.B. Adams, *Nano. Lett.* 2008, **8**, 962-967

18. A. Várez, J. Jolly, P. Oliete, M.L. Sanjuán, E. Garcia-Gonzalez, T. Jardiel and J. Sanz, *Inorg. Chem.*, 2009, **48**, 9693–9699

19. T. Montini, A. Speghini, L. De Rogatis, B. Lorenzut, M. Bettinelli, M. Graziani and P. Fornasiero, *J. Am. Chem. Soc.* 2009, **131**, 13155-13160

20. C. Tiseanu, V. I. Parvulescu, D. Avram, B. Cojocaru, M. Boutonnet and M. Sanchez-Dominguez, *Phys. Chem. Chem. Phys.* 2014, **2**, 703-710.

21. A. Corma, P. Atienzar, H. Garcia and J. Y. Chane-Ching, *Nature Materials* 2004, **3**, 394-397

22. Y. Nagai, T. Yamamoto, T. Tanaka, S. Yoshida, T. Nonaka, T. Okamoto, A. Suda and M. Sugiura, *Catal. Today* 2002, **74**, 225-234

23. J.A. Rodriguez , J.C. Hanson, J.Y. Kim, G. Liu, A. Iglesias-Juez and M. Fernández-García, *J. Phys. Chem. B* 2003, **107**, 3535-3543

24. M. Sanchez-Dominguez, M. Boutonnet and C. Solans, *J. Nanopart. Res*. 2009, **111**, 1823-1829

25. E. Aneggi, C. de Leitenburg, G. Dolcetti and A. Trovarelli, *Catal. Today* 2006, **114**, 40-47

26. M. Yashima, H. Arashi, M. Kakihana and M. Yoshimura, *J. Am. Ceram.Soc.* 1994, **77**, 1067–1071

27. W. Stichert and F. Schüth, *Chem. Mater.* 1998, **10**, 2020-2026

28. G. Chen, N.A. Stump, R.G. Haire and J.R. Peterson, *J. Alloys Compd.*1992, **181**,503-509

29. P. Fornasiero, A. Speghini, R. Di Monte, M. Bettinelli, J. Kašpar, A. Bigotto, V. Sergo and M. Graziani, *Chem.mater*. 2004, **16**, 1938-1944.

30. D. Avram, C. Rotaru, B. Cojocaru, M. Sanchez-Dominguez, M. Florea and C. Tiseanu, *J. Mater. Sci.* 2014, **49**, 2117-2126.

31. C. Tiseanu, B. Cojocaru, V. I. Parvulescu, M. Sanchez-Dominguez, P. A. Primus and M. Boutonnet, *Phys. Chem. Chem. Phys* 2012, **14**, 12970-12981.

32. C.H. Yan, L.D. Sun, C.S. Liao, Y.X. Zhang, Y.Q. Lu, H.S. Huang and S.Z. Lu, *Appl. Phys. Lett.* 2003, **82**, 3511-3513.

33. R. Reisfeld, E. Zigansky and M. Gaft, *Molecular Phys.* 2004, **102**, 1319-1330

34. G. Blasse, A. Brill and W. C. Nieuwpoort, *J. Phys. Chem. Solids* 1966, **27**, 1587-1592

35. C. Görller-Walrand, L. Fluyt, A. Ceulemans and W. T. Carnall, *J. Chem. Phys.* 1991, **95**, 3099-3107

36. R.D. Shannon, *Acta Crystallogr.*1976, **32**, 751–767

37. M. Yashima, *J. Phys. Chem. C* 2009, **113**, 12658–12662

38. P. Li, I.W. Chen and J.E. Penner-Hahn, *Phys. Rev. B* 1993, **48**, 10063-10073

39. C. Tiseanu, V.I. Parvulescu, M. Boutonnet, B. Cojocaru, P. Primus, C. Teodorescu, C. Solans and M. Sanchez - Dominquez, *Phys. Chem. Chem. Phys.* 2011, **13**, 17135-17145

40. A. Kossoy, A. I. Frenkel, Q.Wang, E.Wachtel and I. Lubomirsky, *Adv. Mater.*, 2010, **22**, 1659

41. N. Masanobu and M. Martin, *Phys. Chem. Chem. Phys.*, 2009, **11**, 3241-3249

42. R. McBride, K.C. Hass, B.D. Poindexter and W.H. Weber, *J. Appl.Phys. 1*994,**76**, 2435

43. R. Gerhardt-Anderson and A.S. Nowick, *Solid State Ionics*, 1981, **5**, 547-550

44. D. Y. Wang, D.S. Park, J. Griffith and A.S. Nowick, *Solid State Ionics* 1981, **2**, 95-105

45. V. Bulter, C.R.A. Catlow and B.E.F. Fender, J.H. Harding, *Solid State Ionics*, 1983, **8**, 109

46. X. Wei, W. Pan, L. Cheng and B. Li, *Solid State Ionics*, 2009, **180**, 13-17

47. K. Namjun and J.F. Stebbins, *Chemistry of Materials*, 2007, **19**, 5742-5747

48. C. Tiseanu, V.I. Parvulescu, M. Sanchez-Dominiguez and M. Boutonnet, *J. Appl. Phys.* 2012, **112**, 013521

49. M. Yasima, In *Catalysis by Ceria and Related Materials, 2nd ed., Catalytic Science Series,* (Eds.: A. Trovarelli, P. Fornasiero) 2013, Vol. 12, Chap. 1, Crystal and Electronic Structures, Structural Disorder, Phase Transformation, and Phase Diagram of Ceria–Zirconia and Ceria-Based Materials

50. H. Maekawa, K. Kawata, Y. Ping Xiong, N. Sakai and H. Yokokawa, *Solid State Ionics*, 2009, **180**, 314–319